Materials Characterization 225 (2025) 115109

Contents lists available at ScienceDirect

Materials Characterization

journal homepage: www.elsevier.com/locate/matchar

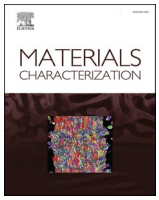

Nanoscale 3D characterization of an Al-1Fe-1Zr alloy for additive manufacturing

Deepak Mani [a,g,*], Peter Cloetens [a], Dmitry Karpov [a], Federico Monaco [a], Bechir Chehab [b], Ravi Shahani [b], Steven Van Petegem [c], Pere Barriobero-Vila [d,e], Katrin Bugelnig [f], Guillermo Requena [f,g]

[a] ESRF-The European Synchrotron, Grenoble 38000, France
[b] Constellium Technology Center, Voreppe 38341, France
[c] Paul Scherrer Institute, PSI Center for Photon Science, Villigen-PSI CH-5232, Switzerland
[d] Technical University of Catalonia (UPC), Department of Materials Science and Engineering, Eduard Maristany Av. 16, Barcelona 08019, Spain
[e] CIM UPC, Carrer de Llorens i Artigas 12, 08028 Barcelona, Spain
[f] German Aerospace Center DLR, Institute of Materials Research, Cologne 51147, Germany
[g] RWTH Aachen University, Aachen 52062, Germany

ARTICLE INFO

Keywords:
Additive manufacturing
Laser powder bed fusion
Aluminium alloy
Phase contrast tomography
X-ray fluorescence tomography

ABSTRACT

The Al-1Fe-1Zr alloy exploits the non-equilibrium solidification dynamics inherent to laser powder bed fusion, characterized by high thermal gradients and rapid solidification front velocities. Here, we investigate the alloy's 3D microstructure using state-of-the-art synchrotron-based nano-tomography techniques. High-resolution holographic and near-field ptychographic X-ray computed tomography were employed, achieving spatial resolutions as small as 57 nm. Our comparative analysis shows that near-field ptychographic tomography offers superior signal-to-noise ratio and spatial resolution, while holographic tomography allows for faster data acquisition with minimal loss in quality. These methods reveal the 3D distribution, morphology, and interconnectivity of Fe-rich and Zr-rich intermetallic phases. Complementary X-ray fluorescence computed tomography further provides quantitative local information on elemental wt%, revealing Fe and Zr distribution with a resolution of 0.1 wt%. The findings highlight key microstructural features that contribute to the alloy's enhanced strength and thermal conductivity, offering critical insights for optimizing its performance in LPBF applications.

1. Introduction

Metal-based additive manufacturing is transforming production strategies in various sectors, including medical, aerospace, transportation, and energy [1–3]. Laser powder bed fusion (LPBF) is a state-of-the-art additive manufacturing technique that enables the production of near-net-shape components with intricate geometries of high precision. This is particularly beneficial in the aerospace industry for the production of metallic components where lightweight designs are crucial. Al alloys are important in this sector because of their strength-to-weight ratio and high corrosion resistance. The aluminium-silicon-magnesium alloys widely used today for LPBF are based on compositions inherited from the shape-casting industry (e.g., AlSi10Mg, F357) [4–6]. These alloys print well but have only moderate mechanical properties. Higher-strength wrought products such as AA6061, AA7050, or AA2195 are susceptible to hot cracking during LPBF [7–9]. The Al-Si-Mg casting alloys and the high-strength wrought alloys are precipitation hardening systems designed to be heat treated by solution treatment, quench, and age [10,11]. The quenching process can lead to distortion of parts [12], which is a major issue for many of the complex geometries targeted by LPBF. Quenching rates can be adjusted to limit the geometric issues, but in general, higher strength alloys require faster quenching rates to reach maximum strength. In addition, even higher quench rates than those necessary for strength are required to avoid grain boundary precipitation, which can negatively impact properties such as intergranular corrosion and toughness. Moreover, these alloys may also have to undergo surface polishing [13,14] to adjust their mechanical properties. Inevitably, in recent years, this has led to the development of new Al alloys designed to take full advantage of LPBF process conditions to produce components with superior overall performance (e.g. [15–17]).

* Corresponding author at: ESRF-The European Synchrotron, Grenoble 38000, France.
E-mail address: deepakmani.esrf@gmail.com (D. Mani).

https://doi.org/10.1016/j.matchar.2025.115109
Received 2 December 2024; Received in revised form 24 February 2025; Accepted 29 April 2025
Available online 2 May 2025

In this context, a novel Al-1Fe-1Zr alloy called Aheadd CP1® by Constellium, specifically tailored to the physical conditions of laser-based additive manufacturing, has recently been introduced to yield better strength and thermal conductivity properties [18]. The alloy shows an increase in yield strength reaching 310 MPa and thermal conductivity of 180 W/m.K after direct ageing for 4 h at 400 °C (YS - 130 MPa and κ - 122 W/m.K in stress-relieved condition) [18,19]. In addition, the alloy demonstrates good LPBF processability by utilizing the high cooling rates taking advantage of high thermal gradients and the solid-liquid interface [18]. The only conventional grades that approach the performance (conductivity-strength balance) of this alloy are the 6xxx series after T6 heat treatments [18]. However, the latter alloys lack LPBF processability, therefore the Al-1Fe-1Zr alloy fills the material property space where complex design, high strength, and conductivity are essential, e.g. for heat exchanger applications.

Both layer-by-layer processing and the melt pools that solidify under the effect of the laser during LPBF manufacturing, usually result in periodic structures along the build direction. Depending on the LPBF processing conditions, microstructural features within these melt pools can vary greatly in terms of grain size, precipitation types, phases formed, etc. [20–22]. Particularly for the Al-1Fe-1Zr alloy studied here, scanning electron microscopy characterization shows the complex grain structures formed during LPBF with a periodicity of ~100-200 μm [18]. Within the melt pools, columnar Al grains are elongated in the direction of solidification, while small equiaxed grains (<10 μm) decorate their boundaries [18]. Pauzon et al. [18] reported that in the fine equiaxed region, Fe is expected to form the $Al_{13}Fe_4$ phase (monoclinic) at the grain boundaries, while Zr forms Al_3Zr primary cubic intermetallics, presumably acting as nucleation sites for the fine equiaxed α-Al grains [18,19].

Although 2D analyses such as electron or optical microscopy, offer valuable information on the microstructures of the alloy, they are inherently limited by its inability to capture the full spatial complexity. Only in recent years has it become possible to investigate the formation of 3D microstructures at the nanoscale non-destructively (e.g. [3,23]). It is essential to probe the intricate microstructure of this novel alloy to gain deeper insights into the presence, type, distribution, and morphologies of microstructural constituents with nanometer resolution and thus to understand the fundamental processes underlying their genesis [3,24]. Here, we present 3D quantitative characterization techniques that can be used to non-destructively analyse the complex internal structure of the new Al-1Fe-1Zr alloy at the nanoscale. The objective of this study is to investigate the ultrafine internal structure, morphology, and mass density of the alloy. This is achieved by employing phase-contrast nanotomography techniques, namely holographic X-ray computed tomography (HXCT) and near-field ptychographic X-ray computed tomography (NFPXCT), available at the ID16A Nano Imaging beamline of the European Synchrotron Radiation Facility (ESRF) [25,26]. In addition, a comparative analysis of the two techniques was conducted with a specific focus on acquisition and reconstruction times, as well as the quality of the reconstructed volumes. To ensure accurate evaluation, all experiments were performed using the same sample and instrumentation. While these techniques provide insight into the internal architecture, particular emphasis is placed on the quantification of elemental distributions by complementary X-ray fluorescence computed tomography (FXCT). The present work provides a unique understanding of the spatial distribution of the microstructures and quantitative local elemental distribution of the amounts of Fe and Zr in the Al matrix.

2. Material and methods

2.1. Material processing

Samples of the Al-1Fe-1Zr alloy were manufactured using a miniaturized LPBF device designed and built at the Paul Scherrer Institute's MicroXAS beamline of the Swiss Light Source (SLS) [27]. The device is optimized for installation at synchrotron beamlines and equipped with the basic functionalities of commercially available LPBF machines. The chamber was continuously flushed with high-purity argon gas to avoid oxygen contamination and the oxygen level was controlled. The samples were produced with a wall geometry of 2 mm × 0.2 mm × 1 mm (*l* x *w* x *h*) and build parameters E = 370 W, hatch = 130 μm, v = 1400 mm/s; layer thickness = 60 μm (thickness = 1–2 hatches), where E is the energy of the laser and v the scanning speed.

A cylindrical sample with a diameter of ~22 μm and a length of ~45 μm was extracted from the additively manufactured wall (Fig. 1 (a)) with a dual beam (electron and Ga^+) FEI Helios Nanolab 600i microscope by focused ion beam (FIB) milling. Prior to FIB milling, platinum coating was deposited on the region of extraction to protect the region of interest from damage. After extraction, the sample was attached to a modified Omniprobe tungsten needle on a Huber sample holder using Pt deposition.

2.2. 3D characterization techniques

The 3D characterization experiments were performed at the ID16A Nano Imaging beamline of the ESRF. The nanotomography techniques available at the beamline are Holographic X-ray Computed Tomography (HXCT) [29] and Near-Field Ptychographic X-ray Computed Tomography (NFPXCT) [30] in the phase contrast domain, providing the electron density distribution of the imaged samples. They are complemented by X-ray Fluorescence Computed Tomography (FXCT) [31] to provide the 3D concentration distributions of individual chemical elements. Designed for hard X-ray imaging techniques, this beamline is well-suited for materials characterization, achieving actual spatial resolutions down to ~30 nm, while still maintaining a relatively large field of view of 30 μm. The beamline operates at two distinct energies: 17.1 keV and 33.35 keV. The X-ray beam is focused into a circular spot of about 20 nm diameter using multilayer-coated fixed curvature Kirkpatrick-Baez (KB) mirrors. In order to cover the two energies of the beamline, two pairs of KB mirrors have been specially designed, as each energy requires an independent KB system. The distance between the source and the focusing element has been fixed at 185 m to obtain a beam with a high degree of spatial coherence. After the focal point, the beam diverges with a well-defined cone geometry and ~ 5mrad divergence in both directions. To scan the sample and correct the run-out errors of the rotation stage, a short-range piezo-driven hexapod and a metrology framework based on twelve capacitive sensors are used. The system ensures the necessary accurate nano-positioning and high stability [32], with translation scanning speeds of 4 and 1 μm/s in the horizontal and vertical directions, respectively. A large vessel under high vacuum (10^{-7}–10^{-8} mbar) houses all the KB nano-focusing optics and the sample stage. The high energy of 33.35 keV was used for the experiments in order to achieve comparably higher spatial resolutions and a reduction of artefacts, while still maintaining a good contrast ratio for phase contrast imaging. Most importantly, it allows excitation of the K-edge of Zr for X-ray fluorescence, resulting in higher efficiency and reduced self-attenuation of the emitted radiation.

2.3. Phase contrast tomography

Both HXCT and NFPXCT are full-field coherent X-ray imaging techniques and share the same experimental setup at ID16A (Fig. 1 (b) and (c)). The projections are recorded with an indirect X-ray detector consisting of a scintillator (20 μm thick Tb doped Lu_2SiO_5 active scintillating layer on a 200 μm thick YbSO substrate), an objective lens (custom-built, 10× magnification with a NA of 0.4) and a XIMEA sCMOS detector with 6144 × 6144 pixels. The optical magnification results in an effective detector pixel size of 1 μm, which was binned by a factor of three, resulting in projections with 2048 × 2048 pixels and a detector pixel size of 3 μm. The detector is positioned at a fixed focus-to-detector distance of $z_{12} = z_1 + z_2 = 1.265$ m. A target pixel size can be selected in the

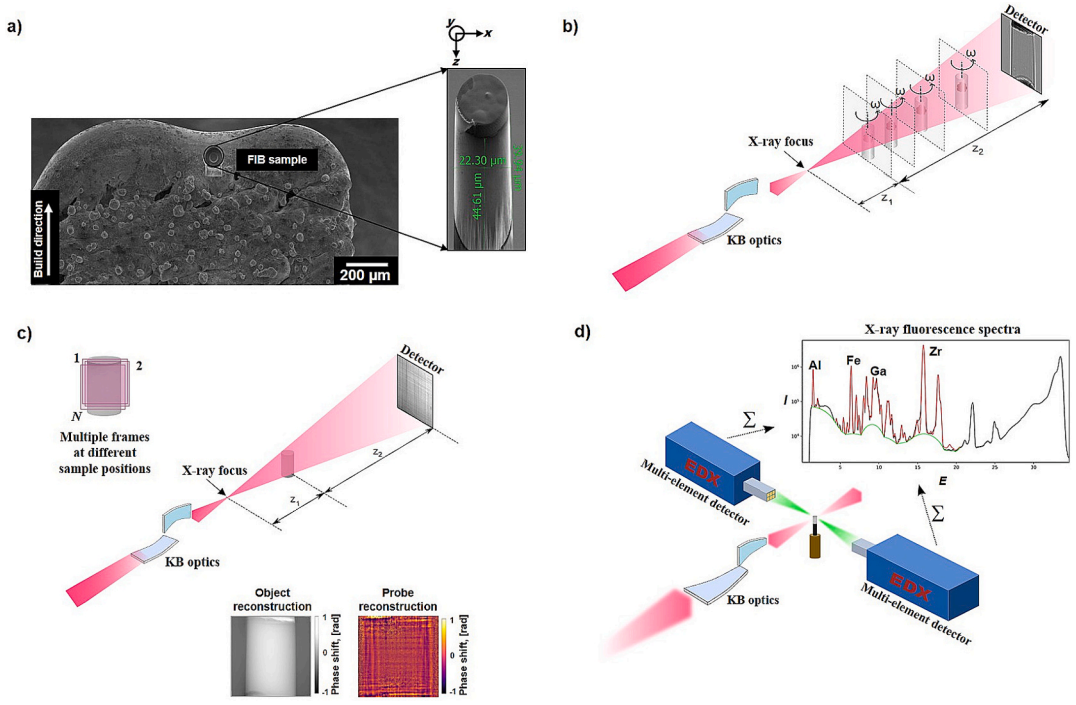

Fig. 1. (a) SEM image of the additively manufactured wall showing the position of the extracted sample (marked in black) for high-resolution 3D characterization. Schematic representation of the different techniques at the ID16A beamline of ESRF (b) Holographic X-ray Computed Tomography (HXCT) [28] (c) Near-field ptychographic X-ray computed tomography (NFPXCT) and (d) X-ray fluorescence computed tomography setup (FXCT). The raw X-ray fluorescence spectra of the extracted sample, summed over the different detector elements are shown.

projections by exploiting the X-ray magnification and positioning the sample along the axis of the divergent cone beam. This produces a phase contrast image on the detector with a geometrical magnification $M = (z_1 + z_2)/z_1$, where z_1 and z_2 are the focus-to-sample distance and the sample-to-detector distance, respectively, along the X-ray beam direction. Specific details of each technique are given below.

2.3.1. Holographic X-ray computed tomography

Holographic X-ray Computed Tomography is an amalgamation of in-line X-ray holography and computed tomography. This technique exploits the magnification effect of the divergent cone geometry of the beam to achieve the required voxel size in the final reconstructed volume [33]. Due to free-space propagation and the high degree of coherence of the beam, the recorded radiographs are actually magnified Fresnel diffraction patterns in the holographic regime, briefly in-line holograms. They contain both attenuation and phase information. Accurate and robust phase retrieval is achieved by combining radiographs recorded at different sample-to-detector distances along the X-ray beam [29]. For this experiment, 4000 projections over 180° are acquired at three focus-to-sample distances with an exposure time of 0.3 s per projection. The first distance with the highest magnification was set at a voxel size of 15 nm, allowing the entire sample to be in the field of view. At each angle, a random lateral motion is added to the sample to avoid ring artefacts in the final reconstructed volume [28]. To perform a flat-field correction, projections without the sample and dark images were recorded at each distance as well. Prior to phase retrieval, the projections at different distances were interpolated to match the pixel size of the first distance and aligned precisely. The phase maps were obtained by an iterative holographic phase retrieval procedure for each angle.

The procedure begins by employing the Paganin methodology [34] presuming the sample is comparatively homogenous. This assumption allows for the evaluation of the ratio of refractive index decrement to absorption coefficient $\delta/\beta \approx 554$ for the alloy at 33.35 keV. An iterative nonlinear conjugate gradient method (CGM) using this estimation as a starting point, enables convergence in a few iterations to a good solution for the phase map at each angle. The phase retrieval is performed with ESRF in-house code using GNU Octave and ImageJ. As a sufficient number of angles were recorded, the tomographic reconstruction was done using the analytic Filtered Back-Projection (FBP) algorithm on the aligned phase maps with the ESRF PyHST2 software [35]. The value provided by the reconstruction is $\omega = -\frac{2\pi}{\lambda}\delta$, where ω is the grey value of the voxel after correction of the offset and δ is the refractive index decrement in the tomogram. The X-ray wavelength λ is calculated from the energy. Assuming the 'Guinier' approximation (Z/A ≈ ½), the grey values in the tomograms are essentially proportional to the mass density of the metallurgical phase [36]. With this approximation, the mass density (ρ) was calculated for each voxel as,

$$\rho\left[g/cm^3\right] = -\frac{10^{-2}\omega[cm^{-1}]}{1.3\lambda\left[\mathring{A}\right]2\pi} \quad (1)$$

2.3.2. Near-field ptychographic X-ray computed tomography

Near-Field Ptychographic X-ray Computed Tomography is an efficient way to retrieve the sample transmission function (object) and the incident illumination function (probe) [37]. Compared to HXCT, this technique can provide higher quality data in terms of signal-to-noise ratio and potentially spatial resolution. A key advantage is that no prior knowledge of sample composition is required, unlike HXCT, which requires to choose the δ/β ratio. However, the acquisition time is longer due to the need to acquire more data. A sequence of holograms is collected at different lateral translations of the sample at a fixed focus-to-sample distance z_1. The structured illumination created by the KB optics is exploited for efficient phase retrieval from the holograms. For this experiment, holograms at 16 lateral pseudo-random positions [37] of the sample were collected with respect to the illumination for each projection angle, where the sample was at a focus-to-sample distance z1 = 6.32 mm that defines the voxel size of 15 nm in the final 3D volume. To avoid residual ring artefacts a random lateral motion was added to

the average sample position at each angle, similar to HXCT [28].

The recorded radiographs are in-line holograms recorded for different transverse shifts of the sample with respect to a structured illumination. A total of 4000 projections were recorded with 4 sub-tomograms, forward and backward over 180° with an exposure time of 0.3 s per radiograph. The phase retrieval was performed with the Python package PyNX [38]. The phase retrieval of the first projection was done using one iteration of Alternating Projections [39] followed by Maximum Likelihood optimization [40] for 4000 iterations while updating the probe. The following projections were started with the previous reconstruction as an initial guess and then improved by Maximum Likelihood optimization [40] for 100 iterations without updating the probe followed by 200 iterations updating the probe. Finally, in order to avoid phase unwrapping, the tomographic reconstruction was carried out on the horizontal derivative of the phase maps using the FBP method with a Hilbert filter [41] with the ESRF in-house software NABU [42]. The calculation of the mass density (ρ) for the volumes is similar to the HXCT method [36].

After deriving the quantitative results from the resulting tomographic volumes, they were further processed for visualization purposes using bandpass filters available in ImageJ [43] to correct for grey value gradients caused by the Pt deposition.

2.4. X-ray fluorescence computed tomography

XRF provides access to elemental concentrations with high efficiency, down to trace elements. The XRF setup uses two energy resolving X-ray detectors based on multi-element Silicon Drift Detector (SSD) technology (Fig. 1 (d)). The first detector is a custom Ardesia-16 detector from Politecnico di Milano [44] consisting of 16 monolithic SDD elements, whereas the second detector is a commercial Vortex ME7 from Hitachi High-Tech Science America consisting of 7 individual SDD elements. At the X-ray focus, the detectors are positioned on either side of the sample, perpendicular to the beam direction in the horizontal plane. The sample is scanned on-the-fly (grid scan) through the nanofocus while the emitted X-ray fluorescence signal is recorded.

Being a scanning method, FXCT is typically orders of magnitude slower than full-field phase imaging methods. To obtain 2D XRF maps the full X-ray fluorescence emission spectra are collected using the energy-dispersive detectors. They are stored for each individual detector element. In addition, a sum spectrum of all detector elements is generated and saved owing to the common energy calibration. The same procedure is repeated for different angular positions of the sample for FXCT. For this experiment, to provide more information about the sample, a region of interest was selected based on the observation of more intra- and intergranular features in the reconstructed phase contrast tomography volumes. A rectangular region, 28 μm wide and 5 μm high was selected and scanned with a grid scan and a step size of 100 nm in the x-y plane. A total number of 65 projections over 180° were acquired with 2 sub-tomograms of 32 projections each and a final projection at 180° to improve the alignment of the projections. This setting provides the best compromise between the target resolution and the field of view, while still having a sufficient number of projections. Taking into account the dwell time of 50 ms for each pixel step and the acquisition overhead time, each projection took ~18 min to acquire, resulting in a total scan time of a little over 20 h.

The spectral fitting and normalization of the XRF data were performed with a Python script using the PyMCA library [45]. The results were 2D maps of the areal mass density (in ng/mm^2) of the different elements in the sample with atomic number $Z > 12$. These projections were then precisely aligned based on the tomographic consistency [46,47]. Contrary to HXCT and NFPXCT, the tomographic reconstruction of each individual element was done using an advanced algebraic reconstruction method – regularized Maximum Likelihood Expectation Maximization (MLEM) [48] implemented with ESRF in-house software using the ASTRA Toolbox [49]. The tomographic voxels provide elemental concentrations in mg/cm^3 by default. To express these concentrations in weight percent (wt%), we first computed the total mass density as the sum of all elemental concentrations (Al, Fe, Zr, and Ga) derived from the FXCT dataset. The relative contribution of each element was then determined through voxel-wise normalization, masked to the region within the object. For the Al matrix, the FXCT result suffers from strong self-attenuation, and instead, a homogeneous density of 2.7 g/cm^3 was assumed. However, the initial Al values were slightly underestimated (~2 g/cm^3). To correct for this, a scaling factor of 1.336 was applied to adjust the Al values to 2.7 g/cm^3. This correction was consistently applied to all other elements to ensure accuracy in the total mass density calculations.

3. Results

3.1. Correlative X-ray nanotomography

To demonstrate the potential of the two full-field coherent imaging techniques, HXCT and NFPXCT, and to accentuate the accuracy of the results, the measurements were carried out with the same voxel size of (15 nm)^3 and 4000 projections with an exposure time of 0.3 s/projection. Fig. 2 shows representative 2D reconstructed slices of the investigated alloy obtained by HXCT (Fig. 2. (a), (e)) and NFPXT (Fig. 2. (b), (f)). The microstructure is formed by the grey Al matrix and bright intermetallic phases that are most likely Fe- and Zr-rich [18]. These phase contrast tomography characterization techniques reveal the morphology, distribution, and interconnectivity of these intermetallic phases decorating fine equiaxed Al grains (<10 μm) (Fig. 2). Fe-rich intermetallics forming an intergranular network at the grain boundaries and the more compact cuboidal Zr-rich primary particles within some of the Al grains are marked in Fig. 2 (a), and can be correlated to those reported in [18,19].

The separate reconstruction of the object (transmission function) and the probe (incident illumination function) in NFPXCT results in improved spatial resolution according to an evaluation by Fourier shell correlation (FSC) (57 nm for NFPXCT and 70 nm for HXCT, see supplementary Fig. S 2). In addition, the reconstruction provides a better signal-to-noise ratio because it does not require the flat-field correction approximation used in HXCT [50]. Nevertheless, the reconstructions produced by HXCT maintain a sufficiently good quality. Fig. 2 (e) shows vertical line artefacts in the axial HXCT slices, whereas NFPXCT is free of such artefacts. Fig. 2 (c) and (g) show enlarged regions of interest from the NFPXCT slice (marked as red and green rectangles in Fig. 2 (b)) in which intermetallic phases with similar morphologies (in 2D) and slight variations in mass density, as revealed by the line profiles in Fig. 2 (d) and (h). The accuracy of the mass density of these microstructural constituents derived from the NFPXCT reconstructions indicates that there may be variations in the composition of these intermetallic phases. Addressing the need for local elemental wt%, FXCT was incorporated as a pivotal factor. As longer acquisitions are required for FXCT, a field of view with a reduced height of 5 μm and a width of 28 μm was selected in a region of interest where more intermetallics were observed in the reconstructed volumes. For a more detailed correlative analysis, the FXCT results in Fig. 3 show the same region as the phase contrast slices in Fig. 2 (a) and (b).

The quantification of individual elements from the FXCT data provides two further insights: 1) The detection of Zr in the Al grains indicates that this element may be either partially trapped in solid solution in the Al matrix or forming nm-range Al_3Zr precipitates, and 2) the presence of Ga decorating Al grain boundaries. Ga was introduced in the alloy during sample preparation by FIB using Ga^+ ions. This element is known to have a high affinity for Al grain boundaries [51], and thus, it can be used as a marker to identify individual grains. Fig. 3 (a) and (b) show axial radial FXCT maps of Zr, Fe, and Ga. The distribution of Zr and Fe in the enlarged regions of interest in Fig. 3 (region enclosed by green and red rectangles in Fig. 3 (b)) confirm the presence of different types of

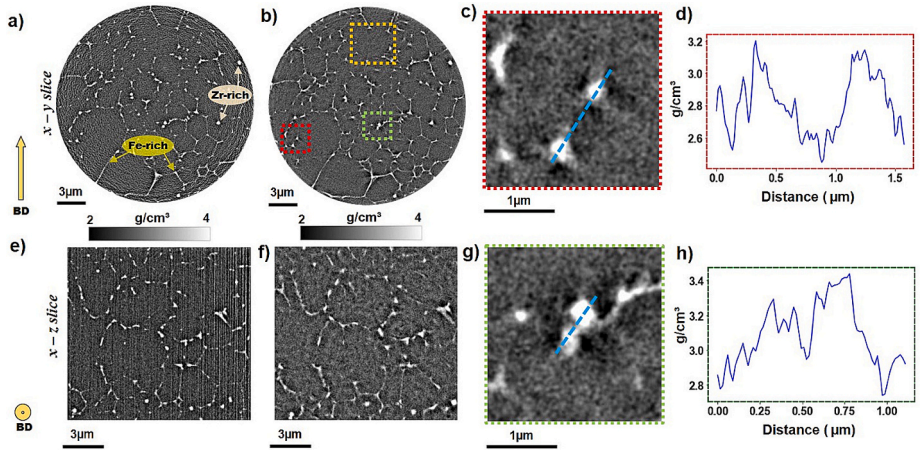

Fig. 2. Comparison between HXCT (a, e) and NFPXCT (b, f) slices of the phase-contrast nano-tomography to reveal the intra/inter granular structures of the Al-Fe-Zr sample. The mass density maps are shown parallel (a and b, contained in the plane of *x-y* slices) and perpendicular (e and f, *x-z* slices) to the building direction (marked BD indicated by gold arrow). The Fe-rich intermetallics and Zr-rich primary particles are shown in (a). The enlarged images in (c) and (g) are highlighted regions of interest in the NFPXCT slice marked in (b, red and green). (d) and (h) are plots of the line profile (marked blue in (c and g)) of the respective regions of interest that indicate the total mass density of the intermetallic phases. (For interpretation of the references to colour in this figure legend, the reader is referred to the web version of this article.)

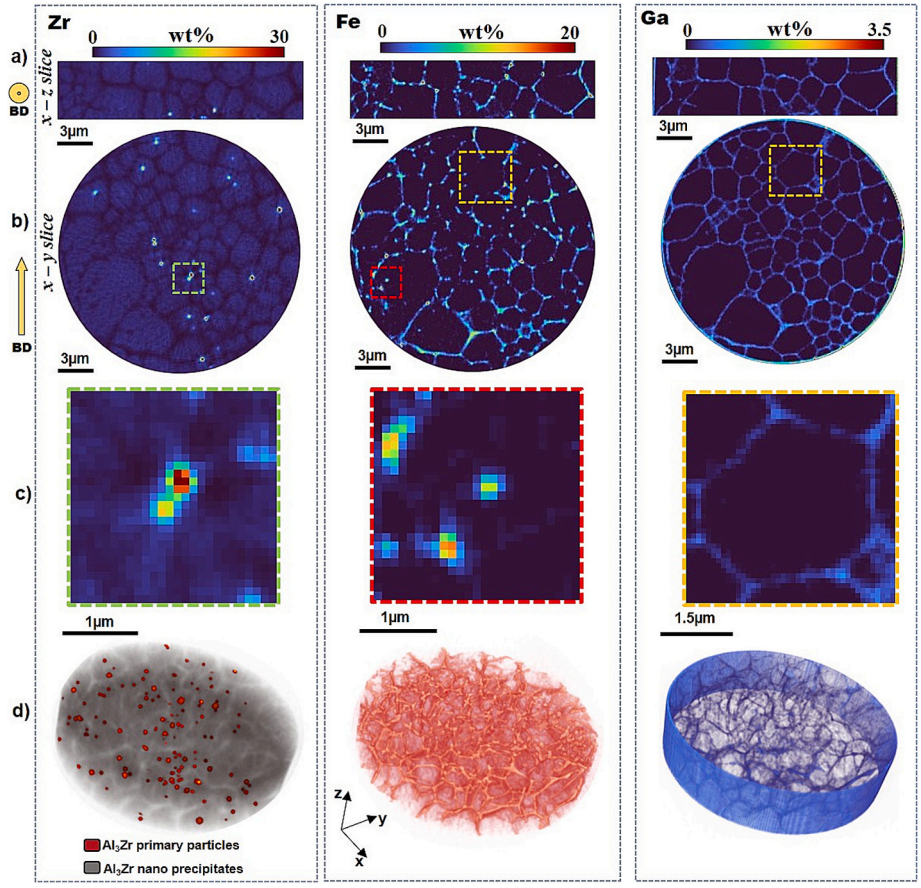

Fig. 3. Orthogonal views of X-ray fluorescence tomography volumes showing the distribution of Zr (left), Fe (middle), and Ga (right). The axial (a) and radial (b) slice (same slice as shown in phase contrast tomography, Fig. 2) reveal the local wt% of the alloying elements Zr and Fe as well as of Ga (introduced as result of sample preparation). Enlarged regions of interest (c) of Zr (marked in green) and Fe (marked in red) corresponding to the regions shown in Fig. 2 (NFPXCT), which indicate they are different intermetallics. The enlarged region of interest of Ga reveals the presence of a grain boundary, with the corresponding region of Fe displaying no observable accumulation of its intermetallics (marked in orange, also refer Fig. 2. b). 3D volume renderings of the elements distributions are shown in (d). (For interpretation of the references to colour in this figure legend, the reader is referred to the web version of this article.)

intermetallic phases despite partly showing a similar 2D morphology and only slight variations in the total mass density (Fig. 2 (d) and (h)). The enlarged region on the right side of Fig. 3 (c) shows Ga clearly decorating a grain boundary, while the same region in the center of Fig. 3 (b) (marked in orange) shows a discontinuous distribution of Fe along this grain. A direct comparison of the elemental content (FXCT), the mass density (NFPXCT) of the three enlarged regions, and 3D visualizations can be found in the Supplementary Fig. S 1 and Movie 1.

Figure 4 (a) show the element distribution and mass density obtained from the FXCT and NFPXCT reconstructions, with a single grain enlarged in Fig. 4 (b). Moreover, the element wt% and mass density along a line profile are shown in Fig. 4 (c). Note the use of a logarithmic scale for the Zr and Fe profiles to exploit the large dynamic range of the reconstructions. The line profile plot of Zr shows a high wt%, most probably a primary Al_3Zr particle, in the center of an Al grain. This particle is surrounded by a uniform distribution of 0.9 wt% of Zr within the Al grain. This uniform distribution is approximately in line with the nominal composition of the alloy. Conversely, the wt% of Fe is higher at the grain boundaries whereas trace amounts of Fe remain trapped in solid solution in the Al grain. Fig. 4 d (left) shows a 3D rendering of the Al grain shown in b, highlighting the heterogeneous distribution of Fe-rich intermetallics at the grain boundary (see also Supplementary movie 2) and the cuboidal Al_3Zr primary particle in the centre of the grain. In the measured FXCT region, the volume fractions of Fe- and Zr-rich intermetallics are 0.23 % and 0.37 %, respectively. The 3D size distribution of the primary Al_3Zr particles within the investigated volume is shown on the right side of Fig. 4 (d). Nearly half of the Al_3Zr particles range between 300 nm and 400 nm in size.

4. Discussion

Focusing on the comparison of HXCT and NFPXCT, one factor to consider is the time needed to acquire the data. The data acquisition time for HXCT is ~4 h, while NFPXCT takes approximately 3 times longer for the same number of projections (4000). This can be explained by the latter method requiring more positions per angle (3 vs 16). Although faster in acquisition and processing time, HXCT requires prior knowledge of the average sample composition to estimate the δ/β ratio for sufficient contrast in the final reconstructed volumes, whereas NFPXCT requires no previous knowledge of the material's composition [30,37]. The reconstruction from NFPXCT achieves a higher spatial resolution, and offers a better signal-to-noise ratio, as it avoids the flat-field correction approximation needed in HXCT. While NFPXCT volumes are devoid of the line artefacts observed in HXCT, a combined wavelet-FFT filter (stripes filter), accessible as the ImageJ plugin, Xlib [52,53], can be applied while processing the HXCT phase maps or to *x*-*z* slices post-reconstruction for the artefact removal. The efficacy of this methodology may be constrained by the severity of the line artefacts [53]. In this case, applying the stripes filter to the HXCT volume preserved the majority of the image information, in addition to the qualitative visual assessment. Nevertheless, NFPXCT results in higher quality volumes with reduced noise and is particularly suitable for samples where noise

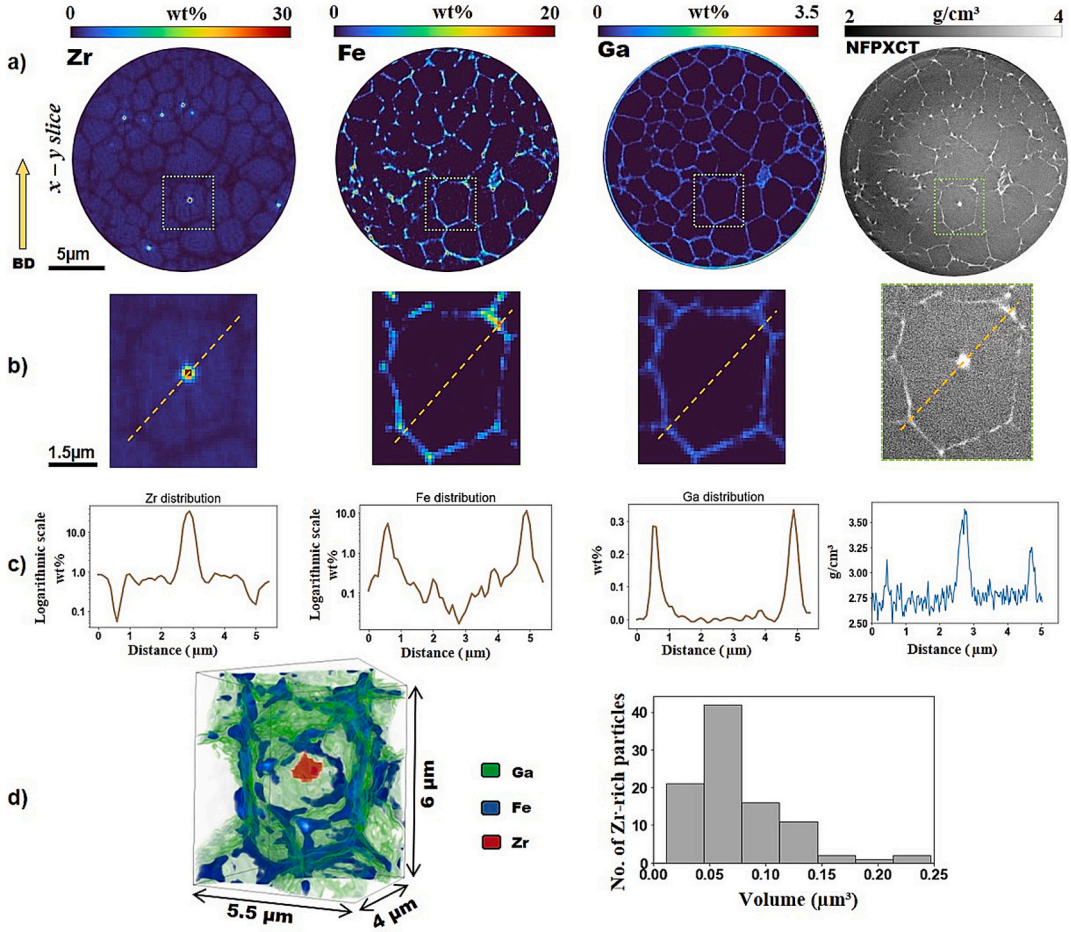

Fig. 4. Quantitative evaluation of an individual grain with FXCT and NFPXCT. (a) Radial slice of elemental maps from FXCT and mass density map retrieved from NFPXCT. (b) Enlarged images of a typical individual grain and (c) line profile plots along a diagonal of the grain tracing the elemental wt% and mass density from FXCT and NFPXT, respectively. (d, left) 3D rendering of the elemental composition of the individual grain (also refer supplementary movie 2), (d, right) histogram for the number of primary Zr-rich particles in the total volume (imaged by FXCT) shown as a function of their volume (μm^3).

can impair analyses. The Supplementary Fig. S 3 illustrates a direct comparison of an *x-z* slice from HXCT volumes before and after applying the stripes filter, alongside the same region of interest from NFPXCT.

These techniques allow qualitative and quantitative 3D characterizations of the Al-1Fe-1Zr microstructure, facilitating the determination of the local mass density of the Al matrix and the intermetallic phases with a spatial resolution of 57 nm and detectability limit of 0.1 g/cm^3 for mass density. However, in the case of phases or regions with similar mass densities, their nature can only be assumed based on other microstructural features such as their 3D morphology. This can still be uncertain, highlighting the significance of FXCT, which yields quantitative local elemental information in 3D (Fig. 3). For the studied alloy, we can precisely quantify each individual element at a voxel size of 100 nm, with a wt% resolution of 0.1 wt% for Zr and Fe, and 0.01 wt% for Ga, within a large dynamic range. This is especially true for the detection of Zr in the Al matrix (which may be trapped in solid solution or forming nm-sized Al_3Zr precipitates). While low vapour pressure and low diffusivity were the main criteria for the selection of the alloying elements in this Al-1Fe-1Zr alloy [18], the role of Zr is twofold: (i) to act as a grain refiner (in the form of primary Al_3Zr particles) to promote heterogeneous nucleation at the melt boundaries to prevent hot cracking [54], and (ii) to act as an age hardening phase that strengthens the alloy owing to nanoprecipitation of coherent Al_3Zr intermetallics during heat treatment [55]. The former can be explained taking into account that the solidification front velocity is the lowest for the liquid that solidifies first, while the thermal gradient decreases from the first solidified liquid to the last [56,57]. As this is sufficiently low at the melt pool boundary, it allows the formation of primary Al_3Zr cuboidal particles (Fig. 4 (d)) that act as nucleation sites for the fine equiaxed Al grains [58]. Furthermore, as the solidification process continues, it may trap Zr in the solid solution if this is slow enough (also indicated by FXCT, Fig. 4). In contrast, the rejection of Fe to the liquid in the peripheral regions of the grains results in the formation of $Al_{13}Fe_4$ intermetallics forming a 3D network that decorates the grain boundaries (Fig. 4). This is also revealed by the Ga distribution which acts as a grain marker in FXCT results (Fig. 4). The theoretical mass densities for Al_3Zr (4.1 g/cm^3 [59–61]) and $Al_{13}Fe_4$ phases (3.8 g/cm^3 [62–64]), were compared with the total mass densities calculated from the FXCT dataset, which were found to be 3.9 g/cm^3 and 3.4 g/cm^3, for Al_3Zr and $Al_{13}Fe_4$ phases, respectively. These values are reasonably close to the expected theoretical densities.

5. Conclusions

The present study demonstrates the strength of different synchrotron-based nanotomography techniques, namely holographic X-ray computed tomography (HXCT) and near-field ptychographic X-ray computed tomography (NFPXCT) and X-ray fluorescence computed tomography (FXCT), to characterize a novel Al-1Fe-1Zr alloy specifically designed for LPBF. The comparative investigations non-destructively reveal the 3D microstructural features down to a spatial resolution of 57 nm, a total mass density resolution of 0.1 g/cm^3 and elemental distribution resolution of 0.1 wt%, depending on the element. The full-field coherent imaging techniques are especially useful for these types of investigations, as they provide a larger field of view and also allow selecting a region of interest for FXCT. The improved spatial resolution of NFPXCT (57 nm vs 70 nm for HXCT) turns out to be particularly relevant considering the size of the ultrafine microstructures in the studied alloy. The results of X-ray phase contrast experiments provided precise mapping and quantification of the microstructures. Combining these techniques with FXCT allows for the unambiguous identification and distribution of the elements and their distribution local wt%.

Supplementary data to this article can be found online at https://doi.org/10.1016/j.matchar.2025.115109.

CRediT authorship contribution statement

Deepak Mani: Writing – original draft, Visualization, Validation, Software, Methodology, Investigation, Formal analysis. **Peter Cloetens:** Writing – review & editing, Validation, Software, Methodology, Investigation, Funding acquisition, Conceptualization. **Dmitry Karpov:** Writing – review & editing, Software, Methodology, Investigation. **Federico Monaco:** Methodology, Investigation. **Bechir Chehab:** Writing – review & editing, Resources, Investigation, Funding acquisition. **Ravi Shahani:** Writing – review & editing, Resources, Investigation, Funding acquisition. **Steven Van Petegem:** Investigation. **Pere Barriobero-Vila:** Investigation. **Katrin Bugelnig:** Writing – original draft, Investigation, Formal analysis. **Guillermo Requena:** Writing – original draft, Methodology, Investigation, Funding acquisition, Conceptualization.

Declaration of competing interest

The authors declare that they have no known competing financial interests or personal relationships that could have appeared to influence the work reported in this paper.

Acknowledgments

This research has been supported by InnovaXN, a EU Horizon 2020 MSCA COFUND programme (innovaxn.eu, grant agreement no. 847439). The ESRF is gratefully acknowledged for the provision of synchrotron facilities at beamline ID16A in the frame of proposals IHMA215 and IHMA354. We acknowledge Frederic Kreps for preparing the sample. The authors would also like to acknowledge the support from Constellium. P.B.-V. acknowledges the financial support from the Spanish Ministry of Science through the Ramón y Cajal grant RYC2020-029585-I. S.V.P. acknowledges financial support from the Swiss ETH domain within the Strategic Focus Area (SFA) Advanced Manufacturing SMARTAM project. We are grateful to Malgorzata Makowska for help with material processing.

Data availability

The primary datasets supporting the findings of this study are publicly available through the European Synchrotron Radiation Facility and can be accessed via the DOI: https://doi.esrf.fr/10.15151/ESRF-DC-2142507587.

References

[1] M. Attaran, The rise of 3-D printing: the advantages of additive manufacturing over traditional manufacturing, Bus. Horiz. 60 (2017) 677–688, https://doi.org/10.1016/j.bushor.2017.05.011.
[2] T. DebRoy, H.L. Wei, J.S. Zuback, T. Mukherjee, J.W. Elmer, J.O. Milewski, A. M. Beese, A. Wilson-Heid, A. De, W. Zhang, Additive manufacturing of metallic components – process, structure and properties, Prog. Mater. Sci. 92 (2018) 112–224, https://doi.org/10.1016/j.pmatsci.2017.10.001.
[3] J. Gussone, K. Bugelnig, P. Barriobero-Vila, J.C. da Silva, U. Hecht, C. Dresbach, F. Sket, P. Cloetens, A. Stark, N. Schell, J. Haubrich, G. Requena, Ultrafine eutectic Ti-Fe-based alloys processed by additive manufacturing – a new candidate for high temperature applications, Appl. Mater. Today 20 (2020) 100767, https://doi.org/10.1016/j.apmt.2020.100767.
[4] J. Gong, K. Wei, M. Liu, W. Song, X. Li, X. Zeng, Microstructure and mechanical properties of AlSi10Mg alloy built by laser powder bed fusion/direct energy deposition hybrid laser additive manufacturing, Addit. Manuf. 59 (2022) 103160, https://doi.org/10.1016/j.addma.2022.103160.
[5] M. Liu, K. Wei, X. Zeng, High power laser powder bed fusion of AlSi10Mg alloy: effect of layer thickness on defect, microstructure and mechanical property, Mater. Sci. Eng. A 842 (2022) 143107, https://doi.org/10.1016/j.msea.2022.143107.
[6] V.A. Medrano, E. Arrieta, J. Merino, B. Ruvalcaba, K. Caballero, B. Ramirez, J. Diemann, L.E. Murr, R.B. Wicker, D. Godfrey, M. Benedict, F. Medina, A comprehensive and comparative study of microstructure and mechanical properties for post-process heat treatment of AlSi7Mg alloy components fabricated in different laser powder bed fusion systems, J. Mater. Res. Technol. 24 (2023) 6820–6842, https://doi.org/10.1016/j.jmrt.2023.04.129.

[7] H. Hyer, L. Zhou, A. Mehta, S. Park, T. Huynh, S. Song, Y. Bai, K. Cho, B. McWilliams, Y. Sohn, Composition-dependent solidification cracking of aluminum-silicon alloys during laser powder bed fusion, Acta Mater. 208 (2021) 116698, https://doi.org/10.1016/j.actamat.2021.116698.

[8] C. Böhm, M. Werz, S. Weihe, Practical approach to eliminate solidification cracks by supplementing AlMg4.5Mn0.7 with AlSi10Mg powder in laser powder bed fusion, Materials 15 (2022) 572, https://doi.org/10.3390/ma15020572.

[9] S. Wu, Z. Lei, B. Li, J. Liang, Y. Chen, Hot cracking evolution and formation mechanism in 2195 Al-Li alloy printed by laser powder bed fusion, Addit. Manuf. 54 (2022) 102762, https://doi.org/10.1016/j.addma.2022.102762.

[10] R.F. Fernandes, J.S. Jesus, R. Branco, L.P. Borrego, J.D. Costa, J.A.M. Ferreira, Influence of post-processing heat treatment on the cyclic deformation behaviour of AlSi10Mg aluminium alloy subjected to laser powder bed fusion, Int. J. Fatigue 164 (2022) 107157, https://doi.org/10.1016/j.ijfatigue.2022.107157.

[11] A. Maamoun, M. Elbestawi, G.K. Dosbaeva, S.C. Veldhuis, Thermal post-processing of AlSi10Mg parts produced by selective laser melting using recycled powder, Addit. Manuf. 21 (2018) 234–247, https://doi.org/10.1016/j.addma.2018.03.014.

[12] A. Ahmed, A. Majeed, Z. Atta, G. Jia, Dimensional quality and distortion analysis of thin-walled alloy parts of AlSi10Mg manufactured by selective laser melting, J. Manufact. Mater. Proces. 3 (2019) 51, https://doi.org/10.3390/jmmp3020051.

[13] F. Scherillo, Chemical surface finishing of AlSi10Mg components made by additive manufacturing, Manufact. Lett. 19 (2018), https://doi.org/10.1016/j.mfglet.2018.12.002.

[14] E. Maleki, S. Bagherifard, F. Sabouri, M. Bandini, M. Guagliano, Hybrid thermal, mechanical and chemical surface post-treatments for improved fatigue behavior of laser powder bed fusion AlSi10Mg notched samples, Surf. Coat. Technol. 430 (2022) 127962, https://doi.org/10.1016/j.surfcoat.2021.127962.

[15] C. Monti, M. Turani, K. Papis, M. Bambach, A new Al-cu alloy for LPBF developed via ultrasonic atomization, Mater. Des. 229 (2023) 111907, https://doi.org/10.1016/j.matdes.2023.111907.

[16] A. Aversa, G. Marchese, A. Saboori, E. Bassini, D. Manfredi, S. Biamino, D. Ugues, P. Fino, M. Lombardi, New aluminum alloys specifically designed for laser powder bed fusion: a review, Materials 12 (2019) 1007, https://doi.org/10.3390/ma12071007.

[17] J.L. Leirmo, High strength Aluminium alloys in laser-based powder bed fusion – a review, Proc. CIRP 104 (2021) 1747–1752, https://doi.org/10.1016/j.procir.2021.11.294.

[18] C. Pauzon, M. Buttard, A. Després, B. Chehab, J.-J. Blandin, G. Martin, A novel laser powder bed fusion Al-Fe-Zr alloy for superior strength-conductivity trade-off, Scr. Mater. 219 (2022) 114878, https://doi.org/10.1016/j.scriptamat.2022.114878.

[19] C. Pauzon, M. Buttard, A. Després, F. Charlot, M. Fivel, B. Chehab, J.-J. Blandin, G. Martin, Direct ageing of LPBF Al-1Fe-1Zr for high conductivity and mechanical performance, Acta Mater. 258 (2023) 119199, https://doi.org/10.1016/j.actamat.2023.119199.

[20] T.-S. Liu, P. Chen, F. Qiu, H.-Y. Yang, N.T.Y. Jin, Y. Chew, D. Wang, R. Li, Q.-C. Jiang, C. Tan, Review on laser directed energy deposited aluminum alloys, Int. J. Extrem. Manuf. 6 (2024) 022004, https://doi.org/10.1088/2631-7990/ad16bb.

[21] J. Su, F. Jiang, J. Teng, L. Chen, M. Yan, G. Requena, L.-C. Zhang, Y.M. Wang, I. V. Okulov, H. Zhu, C. Tan, Recent innovations in laser additive manufacturing of titanium alloys, Int. J. Extrem. Manuf. 6 (2024) 032001, https://doi.org/10.1088/2631-7990/ad2545.

[22] S.R. Narasimharaju, W. Zeng, T.L. See, Z. Zhu, P. Scott, X. Jiang, S. Lou, A comprehensive review on laser powder bed fusion of steels: processing, microstructure, defects and control methods, mechanical properties, current challenges and future trends, J. Manuf. Process. 75 (2022) 375–414, https://doi.org/10.1016/j.jmapro.2021.12.033.

[23] P. Barriobero-Vila, J. Gussone, J. Haubrich, S. Sandlöbes, J.C. Da Silva, P. Cloetens, N. Schell, G. Requena, Inducing stable $\alpha + \beta$ microstructures during selective laser melting of Ti-6Al-4V using intensified intrinsic heat treatments, Materials 10 (2017) 268, https://doi.org/10.3390/ma10030268.

[24] G. Requena, K. Bugelnig, F. Sket, S. Milenkovic, G. Rödler, A. Weisheit, J. Gussone, J. Haubrich, P. Barriobero-Vila, T. Pusztai, L. Gránásy, A. Theofilatos, J.C. da Silva, U. Hecht, Ultrafine Fe-Fe2Ti eutectics by directed energy deposition: insights into microstructure formation based on experimental techniques and phase field modelling, Addit. Manuf. 33 (2020) 101133, https://doi.org/10.1016/j.addma.2020.101133.

[25] J.C. da Silva, A. Pacureanu, Y. Yang, F. Fus, M. Hubert, L. Bloch, M. Salome, S. Bohic, P. Cloetens, High-energy cryo x-ray nano-imaging at the ID16A beamline of ESRF, in: SPIE Optics and Photonics, SPIE, San Diego, CA, United States, 2017 103890F, https://doi.org/10.1117/12.2275739.

[26] J.C. da Silva, A. Pacureanu, Y. Yang, S. Bohic, C. Morawe, R. Barrett, P. Cloetens, Efficient concentration of high-energy x-rays for diffraction-limited imaging resolution, Optica 4 (2017) 492–495, https://doi.org/10.1364/OPTICA.4.000492.

[27] S. Hocine, S. Van Petegem, U. Frommherz, G. Tinti, N. Casati, D. Grolimund, H. Van Swygenhoven, A miniaturized selective laser melting device for *operando* X-ray diffraction studies, Addit. Manuf. 34 (2020) 101194, https://doi.org/10.1016/j.addma.2020.101194.

[28] M. Hubert, A. Pacureanu, C. Guilloud, Y. Yang, J.C. da Silva, J. Laurencin, F. Lefebvre-Joud, P. Cloetens, Efficient correction of wavefront inhomogeneities in X-ray holographic nanotomography by random sample displacement, Appl. Phys. Lett. 112 (2018) 203704, https://doi.org/10.1063/1.5026462.

[29] P. Cloetens, W. Ludwig, J. Baruchel, D. Van Dyck, J. Van Landuyt, J.P. Guigay, M. Schlenker, Holotomography: quantitative phase tomography with micrometer resolution using hard synchrotron radiation x rays, Appl. Phys. Lett. 75 (1999) 2912–2914, https://doi.org/10.1063/1.125225.

[30] M. Stockmar, M. Hubert, M. Dierolf, B. Enders, R. Clare, S. Allner, A. Fehringer, I. Zanette, J. Villanova, J. Laurencin, P. Cloetens, F. Pfeiffer, P. Thibault, X-ray nanotomography using near-field ptychography, Opt. Express, OE 23 (2015) 12720–12731, https://doi.org/10.1364/OE.23.012720.

[31] S. Ünsal, R. Girod, C. Appel, D. Karpov, M. Mermoux, F. Maillard, V.A. Saveleva, V. Tileli, T.J. Schmidt, J. Herranz, Decoupling the contributions of different instability mechanisms to the PEMFC performance decay of non-noble metal O2-reduction catalysts, J. Am. Chem. Soc. 145 (2023) 7845–7858, https://doi.org/10.1021/jacs.2c12751.

[32] F. Villar, L. Andre, R. Baker, S. Bohic, J.C. da Silva, C. Guilloud, O. Hignette, J. Meyer, A. Pacureanu, M. Perez, M. Salome, P. van der Linden, Y. Yang, P. Cloetens, Nanopositioning for the ESRF ID16A Nano-imaging beamline, Synchrotr. Rad. News 31 (2018) 9–14, https://doi.org/10.1080/08940886.2018.1506234.

[33] R. Mokso, P. Cloetens, E. Maire, W. Ludwig, J.-Y. Buffière, Nanoscale zoom tomography with hard x rays using Kirkpatrick-Baez optics, Appl. Phys. Lett. 90 (2007) 144104, https://doi.org/10.1063/1.2719653.

[34] D. Paganin, S. Mayo, T. Gureyev, P. Miller, S. Wilkins, Simultaneous phase and amplitude extraction from a single defocused image of a homogenous object, J. Microsc. 206 (2002) 33–40, https://doi.org/10.1046/j.1365-2818.2002.01010.x.

[35] A. Mirone, E. Brun, E. Gouillart, P. Tafforeau, J. Kieffer, The PyHST2 hybrid distributed code for high speed tomographic reconstruction with iterative reconstruction and a priori knowledge capabilities, Nucl. Instrum. Methods Phys. Res., Sect. B 324 (2014) 41–48, https://doi.org/10.1016/j.nimb.2013.09.030.

[36] A. Diaz, P. Trtik, M. Guizar-Sicairos, A. Menzel, P. Thibault, O. Bunk, Quantitative x-ray phase nanotomography, Phys. Rev. B 85 (2012) 020104, https://doi.org/10.1103/PhysRevB.85.020104.

[37] M. Stockmar, P. Cloetens, I. Zanette, B. Enders, M. Dierolf, F. Pfeiffer, P. Thibault, Near-field ptychography: phase retrieval for inline holography using a structured illumination, Sci. Rep. 3 (2013) 1927, https://doi.org/10.1038/srep01927.

[38] V. Favre-Nicolin, G. Girard, S. Leake, J. Carnis, Y. Chushkin, J. Kieffer, P. Paleo, M.-I. Richard, PyNX: High Performance Computing Toolkit for Coherent X-Ray Imaging Based on Operators, 2020.

[39] S. Marchesini, A. Schirotzek, C. Yang, H. Wu, F. Maia, Augmented projections for ptychographic imaging, Inverse Probl. 29 (2013) 115009, https://doi.org/10.1088/0266-5611/29/11/115009.

[40] P. Thibault, M. Guizar-Sicairos, Maximum-likelihood refinement for coherent diffractive imaging, New J. Phys. 14 (2012) 063004, https://doi.org/10.1088/1367-2630/14/6/063004.

[41] M. Guizar-Sicairos, A. Diaz, M. Holler, M.S. Lucas, A. Menzel, R.A. Wepf, O. Bunk, Phase tomography from x-ray coherent diffractive imaging projections, Opt. Express 19 (2011) 21345–21357, https://doi.org/10.1364/OE.19.021345.

[42] P. Paleo, J. Lesaint, H. Payno, Alessandro mirone, N. Vigano, C. Nemoz, Nabu 2024.1, 2024, https://doi.org/10.5281/zenodo.11104029.

[43] C.A. Schneider, W.S. Rasband, K.W. Eliceiri, NIH image to ImageJ: 25 years of image analysis, Nat. Methods 9 (2012) 671–675, https://doi.org/10.1038/nmeth.2089.

[44] I. Hafizh, G. Bellotti, M. Carminati, G. Utica, M. Gugiatti, A. Balerna, V. Tullio, G. Borghi, A. Picciotto, F. Ficorella, N. Zorzi, A. Capsoni, S. Coelli, L. Bombelli, C. Fiorini, ARDESIA: a fast silicon drift detector X-ray spectrometer for synchrotron applications, X-Ray Spectrom. 48 (2019), https://doi.org/10.1002/xrs.3017.

[45] V.A. Solé, E. Papillon, M. Cotte, Ph. Walter, J. Susini, A multiplatform code for the analysis of energy-dispersive X-ray fluorescence spectra, Spectrochim. Acta B At. Spectrosc. 62 (2007) 63–68, https://doi.org/10.1016/j.sab.2006.12.002.

[46] M. Guizar-Sicairos, J.J. Boon, K. Mader, A. Diaz, A. Menzel, O. Bunk, Quantitative interior x-ray nanotomography by a hybrid imaging technique, Optica 2 (2015) 259–266, https://doi.org/10.1364/OPTICA.2.000259.

[47] J.C. da Silva, J. Haubrich, G. Requena, M. Hubert, A. Pacureanu, L. Bloch, Y. Yang, P. Cloetens, High energy near- and far-field ptychographic tomography at the ESRF, in: Developments in X-Ray, SPIE, Tomography XI, 2017, pp. 39–45, https://doi.org/10.1117/12.2272971.

[48] L.A. Shepp, Y. Vardi, Maximum likelihood reconstruction for emission tomography, IEEE Trans. Med. Imaging 1 (1982) 113–122, https://doi.org/10.1109/TMI.1982.4307558.

[49] W. Van Aarle, W.J. Palenstijn, J. Cant, E. Janssens, F. Bleichrodt, A. Dabravolski, J. De Beenhouwer, K. Joost Batenburg, J. Sijbers, Fast and flexible X-ray tomography using the ASTRA toolbox, Opt. Express 24 (2016) 25129, https://doi.org/10.1364/OE.24.025129.

[50] F. Monaco, M. Hubert, J.C. Da Silva, V. Favre-Nicolin, D. Montinaro, P. Cloetens, J. Laurencin, A comparison between holographic and near-field ptychographic X-ray tomography for solid oxide cell materials, Mater. Charact. 187 (2022) 111834, https://doi.org/10.1016/j.matchar.2022.111834.

[51] L. Lilensten, B. Gault, New approach for FIB-preparation of atom probe specimens for aluminum alloys, PLoS One 15 (2020) e0231179, https://doi.org/10.1371/journal.pone.0231179.

[52] Xlib, ImageJ Wiki (n.d.). https://imagej.github.io/plugins/xlib/index (accessed July 2, 2024).

[53] B. Münch, P. Trtik, F. Marone, M. Stampanoni, Stripe and ring artifact removal with combined wavelet — Fourier filtering, Opt. Express, OE 17 (2009) 8567–8591, https://doi.org/10.1364/OE.17.008567.

[54] X. Li, G. Li, M.-X. Zhang, Q. Zhu, Novel approach to additively manufacture high-strength Al alloys by laser powder bed fusion through addition of hybrid grain refiners, Addit. Manuf. 48 (2021) 102400, https://doi.org/10.1016/j.addma.2021.102400.

[55] S. Bahl, K. Sisco, Y. Yang, F. Theska, S. Primig, L.F. Allard, R.A. Michi, C. Fancher, B. Stump, R. Dehoff, A. Shyam, A. Plotkowski, Al-Cu-Ce(-Zr) alloys with an exceptional combination of additive processability and mechanical properties, Addit. Manuf. 48 (2021) 102404, https://doi.org/10.1016/j.addma.2021.102404.
[56] X. Zhang, B. Mao, L. Mushongera, J. Kundin, Y. Liao, Laser powder bed fusion of titanium aluminides: an investigation on site-specific microstructure evolution mechanism, Mater. Des. 201 (2021) 109501, https://doi.org/10.1016/j.matdes.2021.109501.
[57] P. Van Cauwenbergh, V. Samaee, L. Thijs, J. Nejezchlebová, P. Sedlák, A. Iveković, D. Schryvers, B. Van Hooreweder, K. Vanmeensel, Unravelling the multi-scale structure–property relationship of laser powder bed fusion processed and heat-treated AlSi10Mg, Sci. Rep. 11 (2021) 6423, https://doi.org/10.1038/s41598-021-85047-2.
[58] S. Griffiths, J.R. Croteau, M.D. Rossell, R. Erni, A. De Luca, N.Q. Vo, D.C. Dunand, C. Leinenbach, Coarsening- and creep resistance of precipitation-strengthened Al–Mg–Zr alloys processed by selective laser melting, Acta Mater. 188 (2020) 192–202, https://doi.org/10.1016/j.actamat.2020.02.008.
[59] G. Gautam, A. Mohan, Effect of ZrB2 particles on the microstructure and mechanical properties of hybrid (ZrB2 + Al3Zr)/AA5052 *insitu* composites, J. Alloys Compd. 649 (2015) 174–183, https://doi.org/10.1016/j.jallcom.2015.07.096.
[60] Al3Zr (ZrAl3 m) Crystal Structure - SpringerMaterials, (n.d.). https://materials.springer.com/isp/crystallographic/docs/sd_0261041 (accessed February 21, 2025).
[61] W. Zhang, K. Xu, W. Long, X. Zhou, Microstructure and compressive properties of porous 2024Al-Al3Zr composites, Metals 12 (2022) 2017, https://doi.org/10.3390/met12122017.
[62] P. Pierre Villars, Pearson's Handbook : Crystallographic Data for Intermetallic Phases, Desk ed, ASM International, 1997. https://cir.nii.ac.jp/crid/1130282269714282880 (accessed February 21, 2025).
[63] Al13Fe4 (Fe4Al13) Crystal Structure - SpringerMaterials, (n.d.). https://materials.springer.com/isp/crystallographic/docs/sd_1930868 (accessed February 21, 2025).
[64] J. Gu, S. Gu, L. Xue, S. Wu, Y. Yan, Microstructure and mechanical properties of in-situ Al13Fe4/Al composites prepared by mechanical alloying and spark plasma sintering, Mater. Sci. Eng. A 558 (2012) 684–691, https://doi.org/10.1016/j.msea.2012.08.076.